

Finite-amplitude convection in rotating spherical fluid shells

By A. TILGNER AND F. H. BUSSE

Institute of Physics, University of Bayreuth, D-95440 Bayreuth, Germany

(Received 22 November 1995 and in revised form 26 April 1996)

Finite-amplitude convection in rotating spherical fluid shells is considered for a variety of Prandtl numbers P and Rayleigh numbers Ra up to about 10 times the critical value. Convection at low Rayleigh numbers in the form of azimuthally periodic or weakly aperiodic drifting waves is characterized by relatively low heat transport, especially for $P \lesssim 1$. The transition to strongly time-dependent convection leads to a rapid increase of the heat transport with increasing Rayleigh numbers. Onset of convection in the polar regions is delayed, but contributes a disproportionate fraction of the heat transport at high Rayleigh number. The differential rotation generated by convection, the distributions of helicity, and the role of asymmetry with respect to the equatorial plane are also studied.

1. Introduction

Thermal convection in rotating spherical fluid shells with a spherically symmetric gravity distribution represents one of the fundamental problems in geophysical and astrophysical fluid dynamics. The linear problem of the onset of convection in this configuration is quite well understood now after numerous papers have been devoted to this subject. But the nonlinear problem of finite-amplitude convection in spherical shells has not yet been fully explored. Reasons for the complexity of the problem are that even at the onset of convection the flow is non-axisymmetric and time dependent as was demonstrated by Roberts (1968) and Busse (1970*a*). The problem of the differential rotation generated by non-axisymmetric convection has been a focus of research in the seventies. Weakly nonlinear (Busse 1970*b*, 1973) and fully numerical (Gilman 1977, 1978*a, b*) studies have addressed the question of how various distributions of angular momentum are generated through the actions of Reynolds stresses and meridional circulations. More recently the transition to chaotic motions and the formation of cylindrical layers as proposed by Busse (1976, 1983) have been major topics in the numerical studies of nonlinear convection in rotating spheres (Sun, Schubert, & Glatzmaier 1993*a, b*). But several problems have not yet been well understood, as, for example, the role of the Prandtl number in determining nonlinear properties of convection or the mechanism through which the time dependence of convection leads to a strong enhancement of the heat transport. It is the goal of the present paper to contribute new results to these and other questions.

The paper is organized as follows: We first present the mathematical model and its numerical implementation. Section 3 gives an overview of the observed patterns which are described quantitatively in subsequent sections. These consider in turn the

structure of the convection columns, the longitudinal averages of the velocity and temperature fields, the local heat transport, and global quantities like the Nusselt number and the kinetic energy. Finally, the results are summarized and put into the context of previous work.

2. Mathematical formulation of the problem and numerical methods

We consider a fluid contained in a spherical shell of inner and outer radii \hat{r}_i and \hat{r}_0 . The system is rotating with the angular velocity Ω and constant temperatures are prescribed on the stress-free spherical boundaries. Gravity is assumed to vary linearly with the radius corresponding to an inner core of the same density as the fluid. We introduce a dimensionless description of the problem by using the gap width $d = \hat{r}_0 - \hat{r}_i$ as length scale, d^2/ν as time scale and $P\Delta T$ as temperature scale. The Prandtl number P is defined by $P = \nu/\kappa$, where ν and κ are the viscous and thermal diffusivities. ΔT is the temperature difference between the inner and outer spheres. The equations of motion for the velocity vector \mathbf{u} and the heat equation can now be written in the form

$$\frac{\partial}{\partial t} \nabla \times \mathbf{u} + \nabla \times [(\nabla \times \mathbf{u}) \times \mathbf{u}] = -Ta^{1/2} \nabla \times (\hat{\mathbf{z}} \times \mathbf{u}) + Ra \nabla \times (T\mathbf{r})/r_0 + \nabla^2 \nabla \times \mathbf{u}, \quad (1)$$

$$\nabla \cdot \mathbf{u} = 0, \quad (2)$$

$$\frac{\partial}{\partial t} T + \mathbf{u} \cdot \nabla T = P^{-1} \nabla^2 T, \quad (3)$$

where $\hat{\mathbf{z}}$ is the unit vector along the axis of rotation $\Omega = \Omega \hat{\mathbf{z}}$, the Taylor number Ta is defined as $Ta = (2\Omega d^2/\nu)^2$, and \mathbf{r} is the position vector. The Rayleigh number Ra is given by

$$Ra = \frac{g_0 \alpha \Delta T d^3}{\kappa \nu} \quad (4)$$

where g_0 is the gravitational acceleration at the outer surface and α is the coefficient of thermal expansion. The temperature is now further decomposed as $T = T_s + \Theta$ where Θ stands for the temperature deviation from the profile of pure conduction T_s

$$T_s = -\frac{1 - r_i/r}{1 - r_i/r_0} P^{-1}. \quad (5)$$

The solenoidal velocity field can be written in terms of poloidal and toroidal scalars v and w (Backus 1958)

$$\mathbf{u} = \nabla \times \nabla \times (vr) + \nabla \times (wr). \quad (6)$$

Without losing generality it can be required that the average of v and w over spherical surfaces vanishes. This can be readily seen from the fact that the addition of an arbitrary function of r to either v or w does not change the velocity field \mathbf{u} . We further introduce the representation for v, w , and Θ in terms of spherical harmonics:

$$v = \sum_{l=1}^{\infty} \sum_{m=-l}^l V_l^m(r, t) P_l^m(\theta) e^{im\varphi}, \quad w = r \sum_{l=1}^{\infty} \sum_{m=-l}^l W_l^m(r, t) P_l^m(\theta) e^{im\varphi}, \quad (7a, b)$$

$$\Theta = \sum_{l=0}^{\infty} \sum_{m=-l}^l \Theta_l^m(r, t) P_l^m(\theta) e^{im\varphi}, \quad (7c)$$

where spherical coordinates r, θ, φ have been introduced and where P_l^m denotes the associated Legendre function. The governing equations then reduce to

$$\frac{\partial}{\partial t} W_l^m - \left(D_l - 2 \frac{\partial}{\partial r} \frac{1}{r} \right) W_l^m = \frac{4}{r} \frac{\partial}{\partial r} W_l^m - \frac{1}{l(l+1)} [\mathbf{r} \cdot \nabla \times (\boldsymbol{\Omega}' \times \mathbf{u})]_l^m / r, \quad (8a)$$

$$\frac{\partial}{\partial t} D_l V_l^m - D_l^2 V_l^m = \frac{1}{l(l+1)} [\mathbf{r} \cdot \nabla \times \nabla \times (\boldsymbol{\Omega}' \times \mathbf{u})]_l^m - \frac{Ra}{r_0} \Theta_l^m, \quad (8b)$$

$$\frac{\partial}{\partial t} \Theta_l^m - P^{-1} \left(D_l - \frac{2}{r} \frac{\partial}{\partial r} \right) \Theta_l^m = \frac{1}{P} \frac{2}{r} \frac{\partial}{\partial r} \Theta_l^m - [\nabla \cdot (\mathbf{u} \mathbf{T})]_l^m, \quad (8c)$$

where $\boldsymbol{\Omega}' = \nabla \times \mathbf{u} + Ta^{1/2} \hat{\mathbf{z}}$ and

$$D_l = \frac{\partial^2}{\partial r^2} + \frac{2}{r} \frac{\partial}{\partial r} - \frac{l(l+1)}{r^2}.$$

The boundary conditions are

$$V_l^m = \frac{\partial^2 V_l^m}{\partial r^2} = \frac{\partial W_l^m}{\partial r} = \Theta_l^m = 0 \text{ at } r = r_i \equiv \frac{\eta}{1-\eta} \text{ and at } r = r_o \equiv \frac{1}{1-\eta}. \quad (9)$$

The radius ratio η will be fixed at the value $\eta = 0.4$ in the following analysis. Equations (8) are solved by a spectral Chebychev collocation method. The sums in the representations (7) are truncated to include only terms with $l < L$ and the functions V_l^m, W_l^m and Θ_l^m are expanded in Chebychev polynomials T_n as $\sum_{n=0}^{n_r-1} a_n T_n(x)$ with $x = 2(r - r_i) - 1$. The collocation points in direct space are placed at $r_n = r_i + \frac{1}{2}(1 + \cos \pi(n-1)/(n_r-1))$ with $n = 1, \dots, n_r$, such that a fast cosine transform can be used to switch between physical and spectral space.

Equations (8) are time stepped by treating all terms on the right-hand sides explicitly with an Adams–Bashforth second-order scheme, whereas the terms on the left-hand sides are included in an implicit Crank–Nicolson step. At the beginning of each time step all fields and their first and second radial derivatives are given in (r, l, m) -space; \mathbf{u} and $\nabla \times \mathbf{u}$ are calculated from the poloidal and toroidal fields and transformed into (r, θ, φ) -space. All nonlinear products and the Coriolis term are calculated in physical space. The divergence and radial component of the curl and of the curl of the curl as required in (8) are evaluated with formulas adapted from Glatzmaier (1984).

During the implicit time step a set of n_r linear equations needs to be solved for every pair l, m . The equations determining the variables at the inner- and outermost collocation points are used to enforce the boundary conditions. The corresponding matrices are LU decomposed and stored during initialization. These matrices are arranged to yield Θ, v and w in spectral (n, l, m) -space after the Crank–Nicolson step so that the radial derivatives can then conveniently be obtained and transformed back into (r, l, m) -space together with Θ, v and w for the next time step.

The possibility to fully dealias the nonlinear terms has been included in the code. The resolution of the runs described in this paper was always good enough so that dealiasing did not change the results. Dealiasing the angular variables, however, stabilized the method during transient calculations and at high Ta .

The validity of the code was tested by comparing it to an independently developed Galerkin method. Self-consistency checks have also been made: the heat transport across any spherical surface is the same within 10^{-5} in time-independent states, and the total angular momentum remained negligible throughout all runs, which were started from initial conditions with vanishing angular momentum.

Usually a (possibly remeshed) state obtained at a lower Ra is employed as initial state with some noise added to eliminate spurious symmetries. The adequacy of the resolution has been checked by executing comparative runs with other resolutions. Time integration is continued until a stationary state is reached or enough statistics has been accumulated in the case of chaotic states. The quality of the statistics for any quantity $q(t)$ was judged from the convergence of the running average $Q(t) = (1/t) \int_0^t q(t') dt'$. The variation of $Q(t)$ with time serves as an error estimate. The uncertainties in the results have also been determined through comparisons of runs started from different initial conditions. Yet another error estimate is available for the heat transport: the heat flux averaged over an infinite period of time must be the same across any spherical surface. The variation with the radius of the heat flux averaged over the spherical surface and over a long time span thus provides another error estimate.

At predefined time intervals the program entered a routine computing various quantities of interest for accumulation. These include the Nusselt number Nu ,

$$Nu - 1 = -\eta P \left. \frac{d\Theta_0^0}{dr} \right|_{r=r_i}, \quad (10)$$

the total kinetic energy E_{kin} ,

$$E_{kin} = \frac{1}{2} \int \mathbf{u}^2 dV, \quad (11a)$$

the energies E_{dr} and E_{mc} contained in the differential rotation and in the mean meridional circulation,

$$E_{dr} = \int \sum_l \frac{2\pi}{2l+1} l(l+1) |W_l^0|^2 r^4 dr, \quad (11b)$$

$$E_{mc} = \int \sum_l \frac{2\pi}{2l+1} l(l+1) \{l(l+1) |V_l^0|^2 + |\partial(rV_l^0)/\partial r|^2\} dr, \quad (11c)$$

and the total helicities computed separately for the northern and southern hemispheres,

$$H_{n,s} = \int_{hemisphere} (\nabla \times \mathbf{u}) \cdot \mathbf{u} dV. \quad (12)$$

The helicity $h(r, \theta)$ itself is defined as the azimuthal average $\overline{\mathbf{u} \cdot \nabla \times \mathbf{u}}$ which will also be discussed for various solutions.

3. Flow structure of finite-amplitude convection

In solving the basic equations (8) we have focused on the case $\eta = 0.4$ which represents a good compromise between low η -values and thin fluid shells corresponding to values of η close to unity. In the latter cases the Rayleigh numbers that can be reached with a given computational effort are much lower than for smaller values of η . But $\eta = 0.4$ is not yet small enough that the distinction between polar regions and equatorial regions disappears, which is one of the most distinguishing features of convection in rotating spherical fluid shells.

In order to obtain a rough impression of the conditions for the onset of convection in a rotating spherical fluid shell, it is useful to apply the analytic asymptotic formulas obtained for the case of the cylindrical annulus with stress-free conical end boundaries.

P	Ta	Ra_c	m_c
0.01	10^6	3510	2
0.1	10^6	5580	2
1	0	1133	$l_c = 2$
1	10^6	23200	4
1	10^7	77500	5
10	10^6	34900	6

TABLE 1. P , Ta , Ra_c and m_c for the onset of convection. The uncertainty on Ra_c is $\pm 1\%$

Following the procedure of Busse (1970a, 1982) we find the approximate relationship

$$Ra_c \approx R_a \sin^{-1} \theta_0, \quad m \approx \alpha \hat{r}_0 \sin \theta_0 / D \quad (13)$$

where R_a is the critical Rayleigh number in the annulus case, α is the corresponding wavenumber based on the annular gap width D and θ_0 is the inclination of the conical annular boundaries. The analytical formulas give rise to the following approximate relationships for Ra_c, m_c, ω_c :

$$Ra_c \approx \frac{3\alpha_c^4}{\sin \theta_0} = 3 \left(\frac{DP \sin^{1/4} \theta_0}{\hat{r}_0 \sqrt{2} \cos^2 \theta_0 (1+P)} \right)^{4/3} Ta^{2/3} \approx \frac{3}{2} \left(\frac{4P}{5(1+P)} \right)^{4/3} Ta^{2/3}, \quad (14a)$$

$$m_c = \left(\frac{\hat{r}_0^2 P \sin^4 \theta_0}{D^2 \sqrt{2} \cos^2 \theta_0 (1+P)} \right)^{1/3} Ta^{1/6} \approx \left(\frac{25P}{27 \times 4 \times \sqrt{2} (1+P)} \right)^{1/3} Ta^{1/6}, \quad (14b)$$

$$\omega_c = \left(\frac{D^2 \sin^2 \theta_0 \sqrt{2}}{\hat{r}_0^2 \cos^4 \theta_0 P (1+P)^2} \right)^{1/3} Ta^{1/3} \approx \left(\frac{8\sqrt{2}}{25P(1+P)^2} \right)^{1/3} Ta^{1/3}, \quad (14c)$$

where $D = d$ has been assumed and the expressions on the right-hand sides give the numerical values for $\theta_0 = 30^\circ$. The asymptotic critical value Ra_c is much smaller than the critical values obtained for finite Ta and given in table 1. But since the main purpose of expressions (14) is the elucidation of the dependence on the parameters P and Ta , there is no need for a more detailed adjustment of the parameters of the annulus to the case of the sphere.

As is well known from earlier work on the onset of convection in spherical shells (Busse & Cuong 1977; Zhang & Busse 1987), convection appears first in the equatorial region outside the cylindrical surface touching the inner sphere at its equator. Since the convection flow assumes the form of columns aligned with the axis of rotation, it can be described quite well by the lines of constant z -component of vorticity in the equatorial plane as shown in figure 1. As the Rayleigh number is increased, the stationarily drifting convection columns are replaced by an oscillatory form of convection in which the shape of the columns varies in a time-periodic fashion. Because the slope of the boundaries as well as the mean zonal flow increase with distance from the axis, the phase velocity of the drift tends to be larger for the outer part of the columnar spirals than for the inner part. Thus the outer parts separate from the inner parts in the case of plot (b) and reconnect with the next inner part in the prograde direction as shown in the time sequence of figure 1(d). Since the outer parts of the columns are strongly stretched in a spiral fashion, they require a larger angular region than the inner parts. There are thus twice as many columns on the

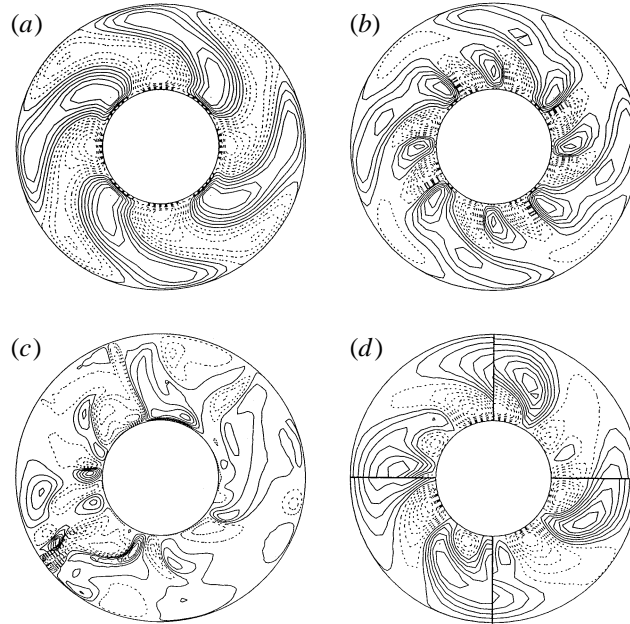


FIGURE 1. Contour plots of the vorticity component ω_z parallel to the axis of rotation in the equatorial plane for $Ta = 10^6$, $P = 1$. Solid (dashed) lines denote positive (negative) values of ω_z . The plots have been obtained for $Ra = 3 \times 10^4$, 8×10^4 , 4×10^5 (*a-c*). Contours of constant Θ in the equatorial plane for four equal distant time steps of $\Delta t = 2.96 \times 10^{-2}$ which cover in the clockwise sense a period of oscillation in the case $Ra = 8 \times 10^4$. The $m = 8$ mode which is predominant near the inner boundary drifts relative to the $m = 4$ mode in the retrograde direction such that a shift by one $m = 8$ wavelength occurs in each period.

inner circle in the case of figure 1(*b*). As the Rayleigh number is increased further, the time-periodic (apart from a shift in azimuth) pattern become chaotic, but the structures seen in figure 1(*c*) still resemble those of the time-periodic case.

The tendency of the convection columns to assume different wavenumbers at different distances from the axis is a general phenomenon of convection in rotating systems with curved boundaries. In the cylindrical annulus system with curved conical boundaries this tendency manifests itself in the form of the double-column instability (Or & Busse 1987) which leads to a break-up of the convection layer into two sub-layers each characterized by convection columns with their own typical wavenumber. Schnaubelt & Busse (1992) have analysed in detail the case of a 2:3 ratio of the wavenumbers. Sun, Schubert & Glatzmeier (1994) show an example of a 5:9 ratio. The 4:8 wavenumber ratio apparent in the plots of figure 1 is special in so far as only the time, not the spatial symmetry is broken in the transition.

When the Taylor number is increased, the number of columns increases as expected from (14*c*) and a similar change of the convection occurs with increasing Ra as has been discussed in connection with figure 1. Typically an asymmetry between areas of cyclonic (solid lines) and anticyclonic vorticity (dashed lines) can be seen which is also noticeable in the plot of figure 1(*c*). Cyclonic vorticity is associated with a flow towards the equatorial plane along the axis of the columns while the opposite flow is associated with anticyclonic columns. The divergence of this component of flow in the equatorial plane tends to widen the cyclonic columns and to stretch the anticyclonic columns as can be seen in figure 1(*b*). At the same time this combination

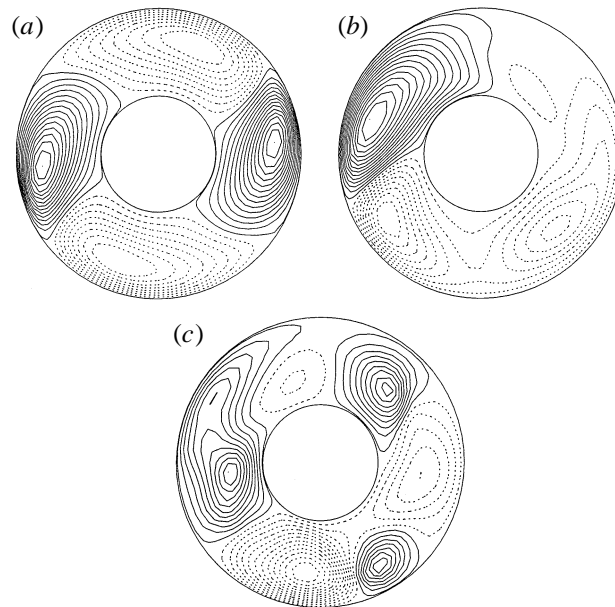


FIGURE 2. Streamlines $-r\partial v/\partial\phi = \text{const.}$ in the equatorial plane for $P = 0.1$, $Ta = 10^6$ and for $Ra = 10^4, 2 \times 10^4, 4 \times 10^4$ (a-c).

of flow and vorticity is responsible for the negative (positive) helicity in the northern (southern) hemisphere. The component along the axis of the columns is a result of the finite inclination of the outer spherical boundary with respect to the equatorial plane as can be understood on the basis of the analytical expressions derived in the case of the rotating cylindrical annulus model (Busse 1975).

For the moderate Prandtl number $P > 1$ the structure of convection does not differ much from that shown in the case $P = 1$ except that small scales in the velocity field are not as easily excited as for $P \leq 1$. The various types of vacillations that can be seen in the weakly nonlinear regime have been studied by Zhang (1991, 1992) in the case $P = \infty$.

At the same Taylor number that has been used for figure 1, convection modes with much lower azimuthal wavenumber become preferred at low Prandtl numbers as is evident from figure 2. The transition from drifting to vacillating columns manifests itself through the interaction of neighbouring modes as for example those with $m = 1, m = 2$ and $m = 3$ in figure 2(b) which gives rise to a periodically varying pattern relative to a drifting frame of reference. As the Rayleigh number is increased further aperiodic distortions of the convection columns occur as is evident in figure 2(c).

The coherence of the convection flow in the direction of the axis of rotation remains preserved to a large extent even as the order in the azimuthal direction disintegrates. The coherence is enforced, of course, by the approximate validity of the Proudman–Taylor condition at high Taylor numbers. But even at the relatively low value of $Ta = 10^6$ the coherence is still a predominant feature at high values of the Rayleigh number as can be seen in figure 3 where the deviation $\Theta - \bar{\Theta}$ of the temperature from its axisymmetric distribution on coaxial cylindrical surfaces has been plotted for several values of Ra . The fact that a minimum of the temperature is usually followed more closely by a maximum in the prograde sense of rotation than in the opposite

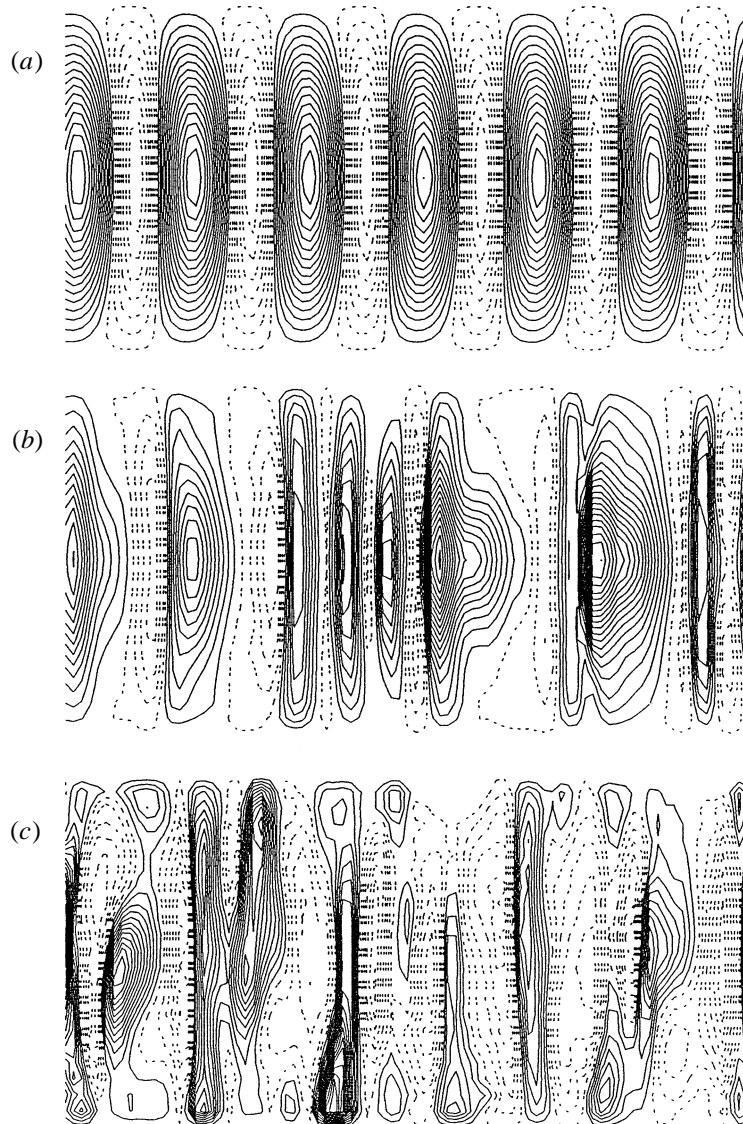


FIGURE 3. Lines of constant temperature deviation from the axisymmetric component, $\Theta - \bar{\Theta}$, on the cylindrical surface $r \sin \theta = 1.168$ in the case $Pr = 10$, $Ta = 10^6$ for $Ra = 4 \times 10^4, 2 \times 10^5, 4 \times 10^5$ (a-c). The angle φ increases from left to right.

case indicates that anticyclonic vortices are narrower than cyclonic ones as we have observed above.

4. Azimuthally averaged properties of convection

Of particular interest are the differential rotation induced by convection and the latitudinal dependence of the heat transport. The differential rotation is generated by the Reynolds stresses of the non-axisymmetric component of convection on the one hand and by the action of the Coriolis force on the meridional circulation on the other hand. For Prandtl numbers P of the order unity or less the differential rotation is

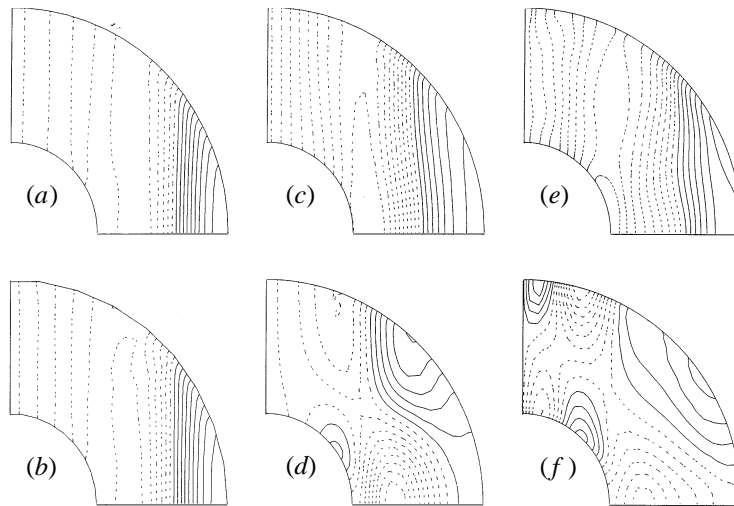


FIGURE 4. Contours of constant azimuthally averaged velocity in the φ -direction, u_φ , for $P = 0.01, Ra = 4.3 \times 10^3$ (a), $P = 0.1, Ra = 7 \times 10^3$ (b), $P = 1, Ra = 5 \times 10^4$ and $Ra = 4 \times 10^5$ (c, e), $P = 10, Ra = 4 \times 10^4$ and $Ra = 4 \times 10^5$ (d, f).

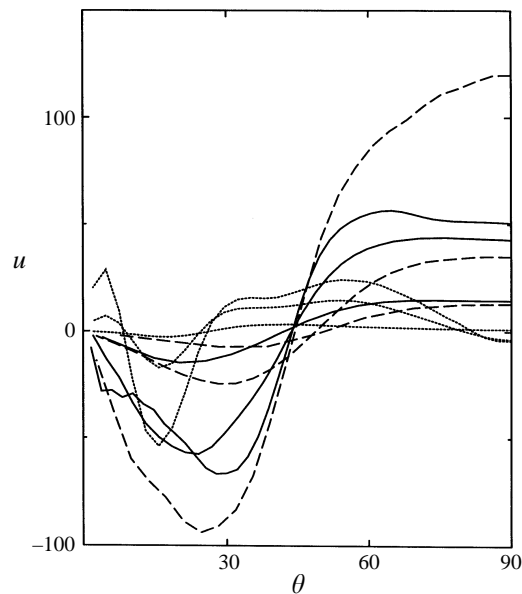


FIGURE 5. The azimuthally averaged φ -component of the velocity field, u_φ , at the surface, $r = r_0$, as a function of the colatitude θ (in degrees) in the case $Ta = 10^6$ for $P = 1$ (solid curves), $P = 0.1$ (dashed lines) and $P = 10$ (dotted lines, curves have been multiplied by a factor 10). The values of u_φ at $\theta = 60^\circ$, increase monotonically with Ra . Curves for $Ra = 10^5, 2 \times 10^5, 4 \times 10^5$ in the case $P = 1$, for $Ra = 10^4, 2 \times 10^4, 4 \times 10^4$ in the case $P = 0.1$ and for $Ra = 7 \times 10^4, 2 \times 10^5, 4 \times 10^5$ in the case $P = 10$ are shown.

nearly in geostrophic equilibrium such that it depends mainly on the distance s from the axis of rotation and little on the z -coordinate in the direction of the axis. This can be seen in figure 4 where only the case $P = 10$ shows significant deviation from the geostrophic balance. The variation of the mean zonal flow at the outer boundary is shown for different Rayleigh and Prandtl numbers in figure 5. As has long been known

P	Ta	Ra	n_r	L	Nu	E_{kin}	E_{tor}	E_{dr}	E_{mc}	H
0.01	10^6	* 4×10^3	17	48	1.00012	1.93×10^3	1.14×10^3	89	0.09	458
		* 4.3×10^3	17	48	1.00016	2.84×10^3	1.62×10^3	208	0.17	638
		° 4.6×10^3	17	48	1.0018	2.05×10^4	9.5×10^3	1.15×10^3	110	7.0×10^3
		5×10^3	17	48	1.0035	4.4×10^4	1.6×10^4	1.16×10^4	125	1.6×10^4
		7×10^3	17	48	1.009	1.5×10^5	4.6×10^4	4.1×10^4	1.5×10^3	5.6×10^4
		1×10^4	17	64	1.025	4.5×10^5	1.75×10^5	1.0×10^5	8.0×10^3	1.22×10^5
		1.5×10^4	17	64	1.050	8.0×10^5	3.75×10^5	5.0×10^4	2.5×10^4	2.0×10^5
0.1	10^6	* 7×10^3	17	16	1.0045	1.24×10^3	744	68	0.036	256
		* 1×10^4	17	16	1.0075	2.75×10^3	1.50×10^3	412	0.167	450
		2×10^4	17	48	1.019	1.31×10^4	6.75×10^3	3.62×10^3	3.94	1.64×10^3
		3×10^4	17	48	1.205	1.18×10^5	5.5×10^4	3.13×10^4	940	1.9×10^4
		4×10^4	17	48	1.34	1.83×10^5	7.15×10^4	5.6×10^4	2.13×10^3	3.7×10^4
		8×10^4	33	64	1.9	5.15×10^5	2.5×10^5	6.3×10^4	1.54×10^4	2.7×10^5
1	10^6	* 3×10^4	17	32	1.06	215	137	27.3	0.014	163
		* 5×10^4	17	32	1.129	810	396	288	0.144	770
		8×10^4	17	32	1.28	2.0×10^3	817	750	1.09	3.85×10^3
		1×10^5	17	32	1.525	5.26×10^3	2.66×10^3	1.3×10^3	3.65	9.1×10^3
		2×10^5	33	64	2.45	2.84×10^4	1.07×10^4	7.5×10^3	103	3.45×10^4
		4×10^5	33	81	4.05	9.0×10^4	4.28×10^4	1.75×10^4	1.0×10^3	1.1×10^5
1	10^7	* 8×10^4	17	64	1.00785	33	23.7	0.785	1.06×10^{-4}	33
		* 1×10^5	17	64	1.0454	310	180	65	5.0×10^{-3}	230
		° 2×10^5	17	64	1.113	1.75×10^3	615	954	0.10	1.75×10^3
		° 3×10^5	17	64	1.165	4.33×10^3	1.18×10^3	2.81×10^3	0.39	4.35×10^3
		4×10^5	33	81	1.4	1.24×10^4	4.63×10^3	5.7×10^3	4.8	2.16×10^4
		6×10^5	33	81	1.7	4.1×10^4	7.8×10^3	2.9×10^4	18	4.5×10^4
		8×10^5	33	81	2.2	8.2×10^4	1.3×10^4	6.4×10^4	52	7.0×10^4
10	10^6	* 4×10^4	17	64	1.0753	2.44	1.82	8.3×10^{-2}	1.33×10^{-4}	4.715
		° 7×10^4	17	81	1.415	20.25	14.4	0.517	0.068	50
		1×10^5	17	64	1.62	40	27	1.26	0.02	110
		2×10^5	17	64	2.5	170	109	7.14	0.21	544
		4×10^5	17	64	3.75	555	260	20.4	2.1	1.54×10^3

TABLE 2. P , Ta , Ra , n_r , L , Nu , E_{kin} , E_{tor} , E_{dr} , E_{mc} , and H for all calculations on the rotating system. A uniformly drifting pattern is observed at the Ra marked by an asterisk. Open circles denote states with time-dependent patterns of longitudinal periodicity m_c (see table 1). The errors on $Nu - 1$ and all other quantities are $\pm 2\%$ in these states. In all other cases, the error is typically $\pm 20\%$ on E_{kin} , E_{dr} , E_{mc} , and H and $\pm 4\%$ on Nu ($\pm 5\%$ on $Nu - 1$ for $Pr = 0.01$)

(Busse 1970*b*), convection tends to generate a prograde differential rotation near the equator, although in the case of moderate or large Prandtl numbers the maximum value of the angular velocity is usually reached at a higher latitude as the Rayleigh number is increased above its critical value. A sharp increase in the retrograde rotation near the poles can be noticed in connection with the onset of convection at the polar regions. At the highest Rayleigh numbers that have been achieved in the numerical simulation the time-averaged differential rotation tends to saturate.

The meridional circulation represents a relatively weak component of the velocity field as is evident from its kinetic energy listed in table 2. Nevertheless, in computations of dynamos even weak meridional circulation may determine the type of dynamo that can be obtained (Roberts 1972; Sarson & Gubbins 1995). Typically the presence

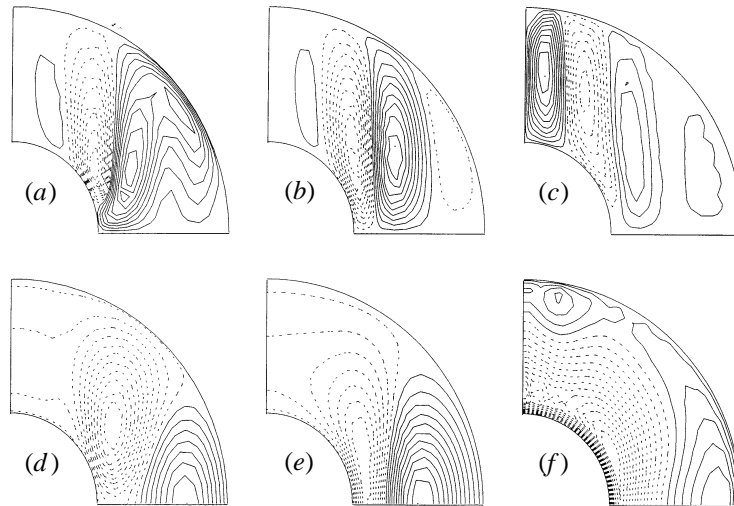


FIGURE 6. Streamlines of the meridional circulation (*a-c*) and contours of constant azimuthally averaged temperature (*d-f*) for $P = 0.01, Ra = 4.3 \times 10^3, P = 1, Ra = 4 \times 10^4, P = 10, Ra = 4 \times 10^5$ (left to right) are shown in the case $Ta = 10^6$.

of a meridional circulation can transform an oscillatory dynamo into a steady one. As shown in figure 6(*a-c*) the meridional circulation also reflects the coherence along coaxial cylindrical surfaces. While at low Rayleigh numbers the polar regions are nearly stagnant, strong circulations set in as soon as a 'critical' Rayleigh number for the onset of convection in the polar regions is exceeded. This onset is not sharply defined, of course, but at about a value of Ra of three to five times the critical value for the equatorial region (Busse & Cuong 1977) the amplitude of convection begins to increase rapidly near the poles. The preferred mode of convection in that region should be in the form of radially directed rolls according to the thin shell analysis of the paper just mentioned. Some indication of this preference can be seen in the plots of figure 7, especially in the plot for $P = 10$.

The axisymmetric component $\bar{\Theta}$ of Θ reflects both the advection by the meridional circulation and the heat transport by the non-axisymmetric component of convection. While significant amplitudes of $\bar{\Theta}$ are confined to the equatorial region for relatively low values of Ra , a nearly spherical symmetric distribution $\bar{\Theta}$ is found at higher values of Ra as can be seen in figure 6(*d-f*). Obviously, after the onset of the polar convection cells the heat transport in these regions soon catches up with the heat transport by equatorial convection as the Rayleigh number is increased.

The change in the style of convection with increasing Rayleigh number is even more evident in plots of the local Nusselt number, $Nu(\theta)$, as a function of the colatitude θ as shown in figure 8. Using the definition

$$Nu_{i,o}(\theta) - 1 = \frac{1}{2\pi} \int_0^{2\pi} \frac{\partial \Theta}{\partial r} d\phi \bigg/ \frac{dT_s}{dr} \quad \text{at } r = r_i, r_o \quad (15)$$

we have plotted the local Nusselt numbers at the inner and outer boundaries, Nu_i and Nu_o , for various Prandtl and Rayleigh numbers. In the case $P = 1$ (see figure 8), the convective part of the heat transport, indicated by $Nu - 1$, assumes only a small fraction of its equatorial value in the polar region as long as the Rayleigh number is

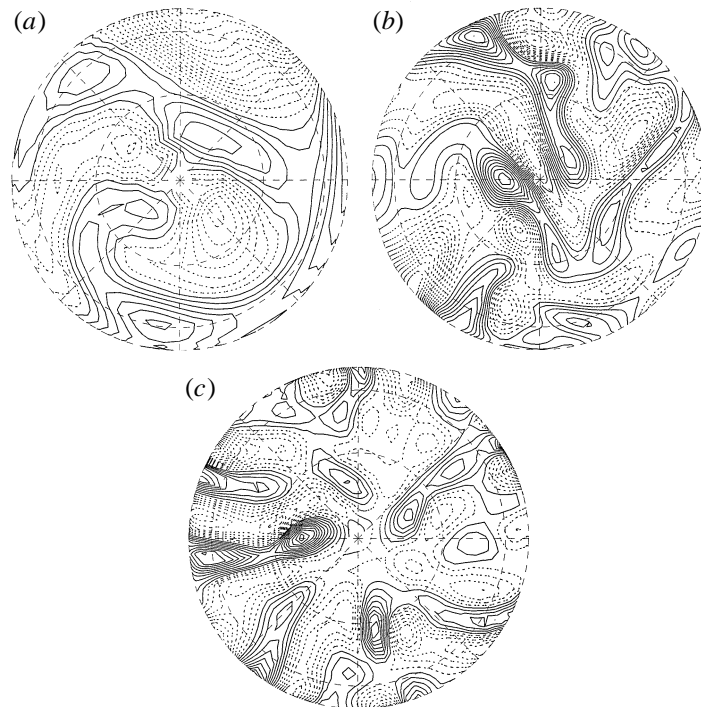


FIGURE 7. Lines of constant radial velocity on the mid-surface $r = (r_i + r_o)/2$ of the fluid shell viewed from the north pole in the case $Ta = 10^6$ for (a) $P = 0.1, Ra = 2 \times 10^4$, (b) $P = 1, Ra = 2 \times 10^5$, (c) $P = 10, Ra = 4 \times 10^5$.

less than about $3Ra_c$. As soon as the convection starts in the polar region, the heat transfer to the inner sphere at the poles increases rapidly with increasing Ra owing to the descending polar plumes. The heat transfer at the outer boundary also increases, but the dependence on θ is more uniform in this case.

In the case of low Prandtl numbers the situation is somewhat more complex. The local Nusselt number Nu_i increases first at the poles relative to its value at the equator as can also be seen in figure 8. But at $Ra = 8 \times 10^4$ the dependence on θ has reversed and Nu_i is now smaller in the polar region than at the equator. The reversal of the direction of the polar plume is responsible for this feature (see figure 9). A corresponding reversal, but less dramatic, is seen in dependence of Nu_o . Although the polar regions seem to be an unlikely place for a maximum of the heat transport per unit area this appears to be the typical situation for low-Prandtl-number fluids.

Figure 9 serves to illustrate another feature of the computations at higher Rayleigh numbers. Although figure 9 has been obtained as a time average over a period of 0.3 thermal time units corresponding to about 60 convection turnover times, there remains a finite asymmetry with respect to the equator which tends to increase slowly with the Rayleigh number. Because of the symmetry of the problem, it must be expected that this asymmetry will disappear for averages over very long intervals. For this reason the arithmetic mean of both hemispheres has been used in all previous figures discussed in this section. Because of the finite computer time available the possibility cannot entirely be excluded that, depending on the initial condition, some amount of asymmetry may persist indefinitely. In the cases

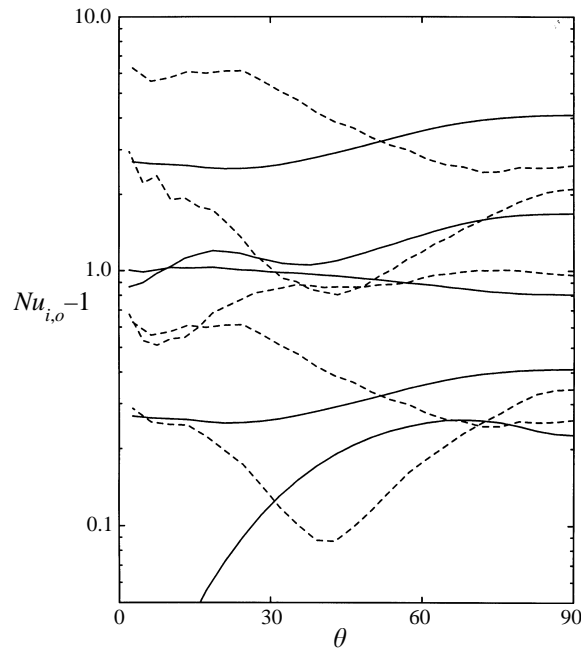


FIGURE 8. The local Nusselt number $Nu_{i,o}$ as a function of the colatitude θ for $Ta = 10^6$ at the inner (solid lines) and the outer (dashed lines) boundary of the fluid shell. The curves correspond to $P = 0.1$ with $Ra = 3 \times 10^4, 4 \times 10^4, 8 \times 10^4$ and to $P = 1$ with $Ra = 2 \times 10^5, 4 \times 10^5$ (from bottom to top at mid-latitudes).

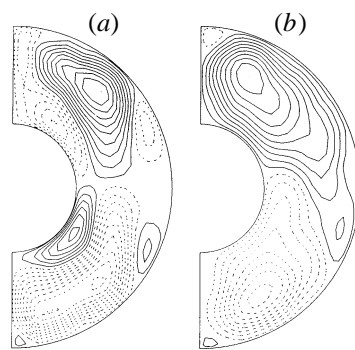


FIGURE 9. Streamlines of the meridional circulation averaged over an interval of length 0.3 in time in the case $Ta = 10^6, P = 0.1$ with $Ra = 4 \times 10^4$ (a) and $Ra = 8 \times 10^4$ (b).

of higher Prandtl number the number of turnover times for time averaging has been less than in the case $P = 0.1$. But at least 4 turnover times have always been used.

The helicity distribution $h(r, \theta)$ is plotted in figure 10 and exhibits the symmetry discussed earlier in that it is predominantly negative in the northern hemisphere while it has the opposite sign in the southern hemisphere. Again a mean value of both hemispheres (including the proper sign) has been plotted in order to approach the expected long-time average. The contribution to the helicity from the axisymmetric components of motions is only of the order of 1% in the case of figure 10.

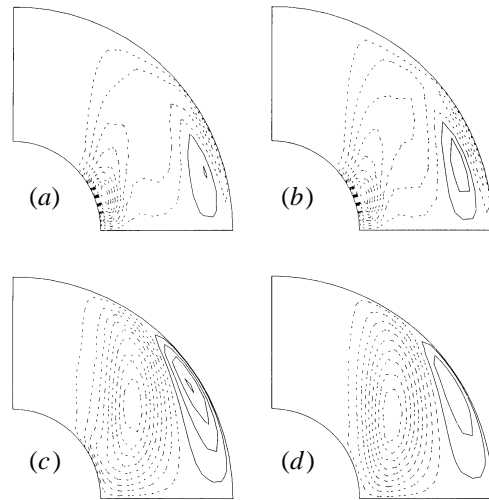


FIGURE 10. Contours of constant helicity $h(r, \theta)$ for $P = 0.01, Ra = 4.3 \times 10^3$ (a), $P = 0.1, Ra = 7 \times 10^3$ (b), $P = 1, Ra = 5 \times 10^4$ (c) and $P = 10, Ra = 4 \times 10^4$ (d), all for $Ta = 10^6$.

5. Global properties of convection

The effects of rotation do not necessarily lead to a decrease in the heat transport by convection. In the case of the cylindrical annulus with parallel end boundaries with convection driven by a radial gravity field (or by centrifugal buoyancy in the case of laboratory experiments) the Coriolis force may actually promote the heat transport through the suppression of three-dimensional motions which exhibit a lower Nusselt number than two-dimensional rolls, at least for Prandtl number of the order unity or less. Even in the case of a horizontal layer rotating about a vertical axis there are parameter regimes for which the heat transport in the presence of rotation is higher than in its absence (Clever & Busse 1979). The influence of the Coriolis force in combination with the geometry of the spherical shell leads to a strong impeding of the convective heat transport, especially at low Prandtl numbers. As can be seen from table 2, at more than 4 times the critical value of the Rayleigh number the Nusselt number is still only about 5% above its static value for $P = 0.01$. In contrast to the horizontal layer, the drifting convection vortices in a spherical shell make it difficult for fluid parcels to travel from the hot to the cold boundary and vice versa. Either the streamlines are strongly extended in a spiral fashion and the drift may reverse the motion of the parcel before it has travelled very far, or the dimension of convection columns in the direction perpendicular to the axis is too small, or the convection is attached to outer equatorial boundary as in the case of figure 5 and even more so at lower Prandtl number (Zhang & Busse 1987).

In the case of the Prandtl numbers $P = 0.1$ and $P = 1$ a rather sudden change in slope in the $Nu(Ra)$ -relationship can be noticed in figure 11 which is connected with the onset of a strong time dependence of convection. Since a weak time dependence, apart from the general drift, can already be noticed at Rayleigh numbers not far above the critical value it is not easy to pinpoint the mechanism through which chaotic convection leads to the strong increase in the convective heat transport. This phenomenon has been studied in detail in the case of convection in a cylindrical annulus where the transition from the stationary

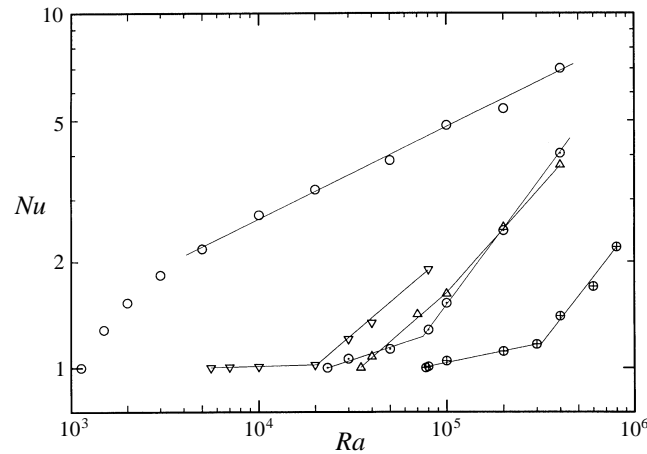


FIGURE 11. The dependence-time of averaged Nusselt number Nu on the Rayleigh number Ra for $Ta = 0, P = 1$ (\circ), for $Ta = 10^6, P = 0.1$ (∇), $P = 1$ (\circ), $P = 10$ (Δ) and for $Ta = 10^7, P = 1$ (\oplus).

mean flow solution to vacillating convection yields a similarly strong change in the slope of the $Nu(Ra)$ -dependence (Or & Busse 1987; Schnaubelt & Busse 1992). Only at Prandtl numbers of the order 10 or larger is the slope of the $Nu(Ra)$ -curve at $Ra = Ra_c$ comparable to that of the non-rotating case. The slope even exceeds the slope of the non-rotating case. This feature can also be noticed in the case of a plane layer with vertical axis of rotation (Veronis 1968; Clever & Busse 1979) because convection with small horizontal wavelength (which is preferred in the rotating case) is more effective in transporting heat than large-wavelength convection.

The plots of the kinetic energy versus Rayleigh number shown in figure 12 only partly reflect the kinks that have just been discussed in connection with figure 11. In the case $P = 1$ the kinetic energy grows smoothly with the Rayleigh number and only in the case $P = 0.1$ is a jump in the kinetic energy seen at about the same Rayleigh number where the slope of the $Nu(Ra)$ -dependence changes.

While figures 11 and 12 present only time-averaged properties, there is much to be learnt from the correlations in time between the global properties. These are most easily studied at low Rayleigh numbers, in the regime of (nearly) periodic time dependence. As is evident from figure 13 differential rotation and heat transport as given by the Nusselt number are anti-correlated in time for Prandtl numbers much less than unity. The shearing due to the differential rotation tends to inhibit convective motions and the maximum of the energy of the axisymmetric component of the toroidal part of the velocity thus nearly coincides with the minimum of Nu . The energy of the poloidal part of the velocity field, on the other hand, is well correlated with the convective heat transport. The shearing action of the differential rotation decreases with increasing Prandtl number and the anticorrelation with the heat transport changes into a positive correlation as the Prandtl number begins to exceed unity. Because the period of vacillations becomes longer, the sustenance of differential rotation against viscous dissipation depends on a sufficiently strong amplitude of convection for large P , which explains the change in the correlation.

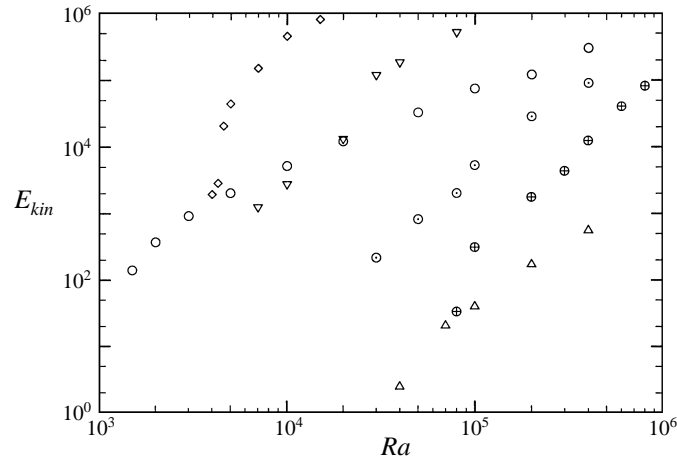


FIGURE 12. The time-dependence of averaged kinetic energy of the convection flow on the Rayleigh number Ra for $Ta = 0, P = 1$ (\circ), for $Ta = 10^6, P = 0.01$ (\diamond), $P = 0.1$ (∇), $P = 1$ (\circ), $P = 10$ (Δ) and for $Ta = 10^7, P = 1$ (\oplus).

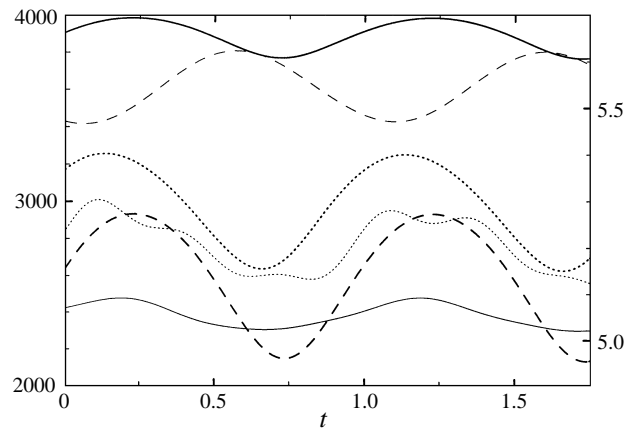


FIGURE 13. Nusselt number Nu (solid lines), kinetic energy of differential rotation, E_{dr} , (dashed lines), kinetic energy, E_{pol} , of the non-axisymmetric component of the poloidal component of motion (dotted lines) for $P = 0.1, Ta = 10^6, Ra = 2 \times 10^4$ (thin lines, left ordinate) and for $P = 10, Ta = 10^6, Ra = 7 \times 10^4$ (thick lines, right ordinate). The time is measured in units of the periods of oscillations which is 0.0241 (3.22) for the case of $P = 0.1$ (10). The Nusselt number measured on the left (right) ordinate has been multiplied by the factor 2000 (4). E_{dr} measured on the right ordinate (thick dashed line) has been multiplied by the factor 10.

6. Concluding discussion

A previous analysis (Zhang & Busse 1987) of the linear problem of the onset of convection in rotating spherical shells has already emphasized the importance of the Prandtl number for solutions of the problem. While the onset of convection occurs in a similar manner for Prandtl numbers of the order unity or larger, different modes of convection compete at low Prandtl numbers. In the present paper the nonlinear properties of convection show a similar behaviour. The style of convection is quite different for low and for moderate to large Prandtl numbers with the case

of $P = 1$ assuming a special role in that it straddles the boundary between low- and high-Prandtl-number convection.

Because of the relative large number of parameters entering the problem and because of the high demand on computer capacities especially for low Prandtl number solutions, various aspects of finite-amplitude convection could not be investigated. The transition from equator-attached to columnar convection (Zhang & Busse 1987) has not been studied at finite-amplitudes and the relationship to inertial-wave-type convection at very low Prandtl numbers (Zhang 1994) has not been analysed either. Some of the features found in the properties of turbulent convection, such as kinks in the Nusselt number dependence on Ra , can eventually be understood more clearly when a bifurcation theory is applied to a reduced system of modes generated, for example, through the imposition of azimuthal periodicity. Evidently the irregular wandering of fluid columns facilitates the movement of hot and cold fluid to the boundary of opposite temperature.

The origin of the equatorial asymmetry is also incompletely understood and will require additional analysis based on stability studies of special solutions. In full numerical simulations such as those described in the present paper it is difficult to isolate the physical mechanisms leading to small asymmetries.

The research reported in the paper has been supported by the Deutsche Forschungsgemeinschaft under Grant Bu589/5-2. The authors are grateful to Dr J. Wicht for his help in checking the numerical code against his Galerkin code.

REFERENCES

- BACKUS, G. E. 1958 A class of self sustaining dissipative spherical dynamos. *Ann. Phys.* **4**, 372–447.
- BUSSE, F. H. 1970*a* Thermal instabilities in rapidly rotating systems. *J. Fluid Mech.* **44**, 441–460.
- BUSSE, F. H. 1970*b* Differential rotation in stellar convection zones. *Astrophys. J.* **159**, 629–639.
- BUSSE, F. H. 1973 Differential rotation in stellar convection zones II. *Astron. Astrophys.* **28**, 27–37.
- BUSSE, F. H. 1975 A model of the geodynamo. *Geophys. J. R. Astron. Soc.* **42**, 437–459.
- BUSSE, F. H. 1976 A simple model of convection in the Jovian atmosphere. *Icarus* **20**, 235–260.
- BUSSE, F. H. 1982 Thermal convection in rotating systems. *Proc. Ninth US Natl Congr. of Applied Mechanics*, pp. 29–305. ASME.
- BUSSE, F. H. 1983 A model of mean zonal flow in the major planets. *Geophys. Astrophys. Fluid Dyn.* **23**, 153–174.
- BUSSE, F. H. & CUONG, P. G. 1977 Convection in rapidly rotating spherical fluid shells. *Geophys. Astrophys. Fluid Dyn.* **8**, 17–44.
- CLEVER, R. M. & BUSSE, F. H. 1979 Nonlinear properties of convection rolls in a horizontal layer rotating about a vertical axis. *J. Fluid Mech.* **94**, 609–627.
- GILMAN, P. A. 1977 Nonlinear dynamics of Boussinesq convection in deep rotating spherical shells - I. *Geophys. Astrophys. Fluid Dyn.* **8**, 93–136.
- GILMAN, P. A. 1978*a* Nonlinear dynamics of Boussinesq convection in deep rotating spherical shells - II: Effects of temperature boundary conditions. *Geophys. Astrophys. Fluid Dyn.* **11**, 157–179.
- GILMAN, P. A. 1978*b* Nonlinear dynamics of Boussinesq convection in deep rotating spherical shells - III: Effects of velocity boundary conditions. *Geophys. Astrophys. Fluid Dyn.* **11**, 181–203.
- GLATZMAIER, G. A. 1984 Numerical simulations of stellar convective dynamos. I. The model and the method. *J. Comput. Phys.* **55**, 461–484.
- OR, A. C. & BUSSE, F. H. 1987 Convection in a rotating cylindrical annulus. Part 2. Transitions to asymmetric and vacillating flow. *J. Fluid Mech.* **174**, 313–326.
- ROBERTS, P. H. 1968 On the thermal instability of a rotating-fluid sphere containing heat sources. *Phil. Trans. R. Soc. Lond. A* **263**, 93–117.
- ROBERTS, P. H. 1972 Kinematic dynamo models. *Phil. Trans. R. Soc. Lond. A* **272**, 663–698.

- SARSON, G. R. & GUBBINS, D. 1996 Three-dimensional kinematic dynamos at high magnetic Reynolds number. *J. Fluid Mech.* **306**, 223–245.
- SCHNAUBELT, M. & BUSSE, F. H. 1992 Convection in a rotating cylindrical annulus. Part 3. Vacillating and spatially modulated flows. *J. Fluid Mech.* **245**, 155–173.
- SUN, Z.-P., SCHUBERT, G. & GLATZMAIER, G. A. 1993a Transitions to chaotic thermal convection in a rapidly rotating spherical fluid shell. *Geophys. Astrophys. Fluid Dyn.* **69**, 95–131.
- SUN, Z.-P., SCHUBERT, G. & GLATZMAIER, G. A. 1993b Banded surface flow maintained by convection in a model of the rapidly rotating Giant Planets. *Science* **260**, 661–664.
- SUN, Z.-P., SCHUBERT, G. & GLATZMAIER, G. A. 1994 Numerical simulations of thermal convection in a rapidly rotating spherical shell cooled inhomogeneously from above. *Geophys. Astrophys. Fluid Dyn.* **75**, 199–226.
- VERONIS, G. 1968 Large-amplitude Bénard convection in a rotating fluid. *J. Fluid Mech.* **31**, 113–139.
- ZHANG, K. 1991 Vacillatory convection in a rotating spherical fluid shell at infinite Prandtl number. *J. Fluid Mech.* **228**, 607–628.
- ZHANG, K. 1992 Convection in a rapidly rotating spherical shell at infinite Prandtl number: transition to vacillating flows, *Phys. Earth Planet. Inter.* **72**, 236–248.
- ZHANG, K. 1994 On coupling between the Poincaré equation and the heat equation. *J. Fluid Mech.* **268**, 211–229.
- ZHANG, K. & BUSSE, F. H. 1987 On the onset of convection in rotating spherical shells. *Geophys. Astrophys. Fluid Dyn.* **39**, 119–147.